

A Semiconductor Topological Photonic Ring Resonator

M. Jalali Mehrabad,^{1, a)} A.P. Foster,^{1, b)} R. Dost,¹ E. Clarke,² P.K. Patil,² I. Farrer,³ J. Heffernan,³ M.S. Skolnick,¹ and L.R. Wilson¹

¹⁾Department of Physics and Astronomy, University of Sheffield, Sheffield S3 7RH, UK

²⁾National Epitaxy Facility, University of Sheffield, Sheffield S1 4DE, UK

³⁾Department of Electronic and Electrical Engineering, University of Sheffield, Sheffield S1 4DE, UK

(Dated: 13 April 2022)

Unidirectional photonic edge states arise at the interface between two topologically-distinct photonic crystals. Here, we demonstrate a micron-scale GaAs photonic ring resonator, created using a spin Hall-type topological photonic crystal waveguide. Embedded InGaAs quantum dots are used to probe the mode structure of the device. We map the spatial profile of the resonator modes, and demonstrate control of the mode confinement through tuning of the photonic crystal lattice parameters. The intrinsic chirality of the edge states makes them of interest for applications in integrated quantum photonics, and the resonator represents an important building block towards the development of such devices with embedded quantum emitters.

The integration of quantum photonic elements on chip presents a highly promising route to the realisation of scalable quantum devices. A key requirement of such an approach is the development of optical waveguides exhibiting low loss and negligible back scatter.¹ Recently, topological waveguides have emerged as a new class of photonic device enabling the robust propagation of light on chip.^{2–10} At the interface between two topologically-distinct photonic crystals (PhCs), counter-propagating edge states of opposing helicity arise, which are ideal for optical waveguiding.^{5,10–13} Significant developments in this field include the demonstration of efficient guiding of light around tight corners,^{4,14–16} robust transport despite the presence of defects,¹⁷ and integration with passive optical elements including nanobeam waveguides¹⁵ and grating couplers.⁴ Compatibility with embedded quantum emitters such as quantum dots (QDs) has been demonstrated, and used to probe the waveguide transmission.^{4,14} Recently, chiral coupling of a QD to a topological waveguide was demonstrated.^{4,18} This is a result of the intrinsic helicity of the edge states and is of great interest for chiral quantum optics.¹⁹

Here, we use a spin Hall-type topological waveguide to create a GaAs topological photonic ring resonator, and probe its mode structure using embedded InGaAs QDs. We map the spatial dependence of the confined modes of the resonator, and demonstrate that perturbation of the PhC lattice can be used to tune the lateral confinement of the modes.

A schematic of the PhC forming the basis of our topological ring resonator is shown in Fig. 1a. The unit cell of the PhC consists of six triangular air holes of side length s , etched into a GaAs membrane of thickness h . A two-dimensional PhC lattice is created using a hexagonal array of unit cells with period $a = s/0.31$.

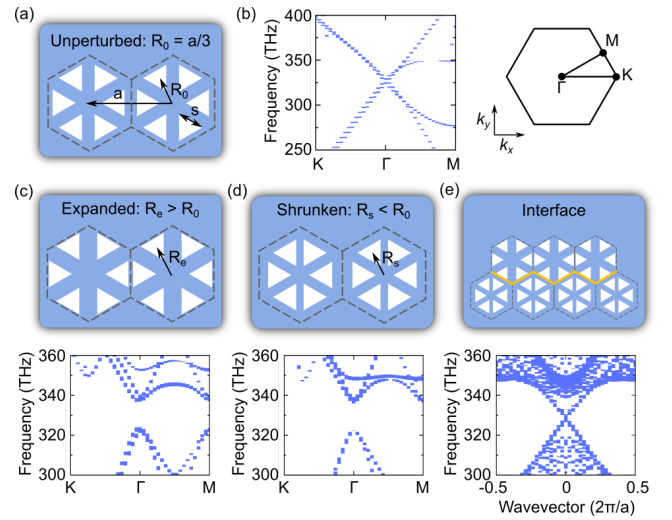


FIG. 1. (a) Schematic showing two unit cells of an unperturbed topological photonic crystal (PhC). The triangles represent air holes. A two-dimensional PhC is formed using a triangular lattice of unit cells, with pitch a . (b) Band structure of the unperturbed lattice, revealing a Dirac cone at the Γ point. Points of high symmetry in the Brillouin zone are shown in the schematic to the right. (c,d) Schematic of (c) expanded and (d) shrunken unit cells. The band structure for a PhC formed from such a unit cell is also shown. In each case a bandgap is opened at the Γ point. (e) Schematic of an interface formed between expanded and shrunken unit cells. Edge modes are seen to cross the bandgap in this case. The parameters used for the band structure calculations were refractive index = 3.4, $h=170\text{nm}$, $s=140\text{nm}$, $a=445\text{nm}$, $R_e=156\text{nm}$ and $R_s=141\text{nm}$.

A key parameter of the lattice is the distance R from the origin of the unit cell to the centre of each triangular aperture, with a graphene-like structure formed when $R = R_0 = a/3$. We model the structure using a commercially available 3D finite-difference time-domain (FDTD) electromagnetic simulator²⁰, and show that in this case the PhC band structure exhibits a Dirac cone at the Γ

^{a)}mjalalimehrabad1@sheffield.ac.uk

^{b)}andrew.foster@sheffield.ac.uk

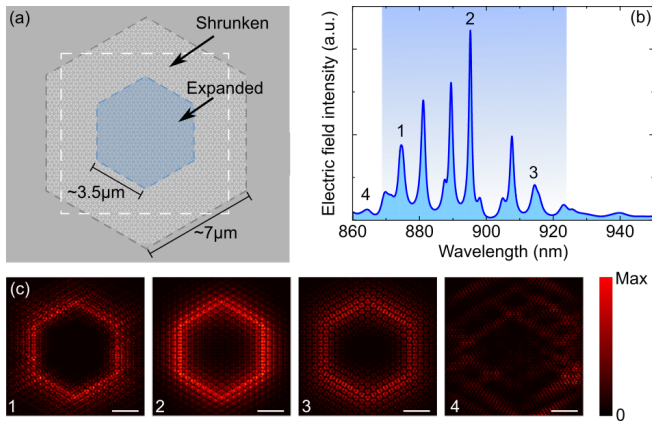


FIG. 2. (a) Schematic of the ring resonator. (b) Mode spectrum at the resonator interface, determined using FDTD simulation. Fabry-Pérot modes can be seen within the topological bandgap (shaded). (c) Spatially-resolved electric field intensity (linear scale) in the plane of the device, for the modes labelled in (b). For modes within the bandgap (panels 1-3), confinement of light at the interface is clearly seen. No interface mode is observed outside of the bandgap (panel 4). The electric field intensity is evaluated within the white dashed region in (a). Scale bar $2\mu\text{m}$.

point, as shown in Fig. 1b.

However, when a perturbation is introduced such that $R \neq a/3$, a bandgap is opened at the Γ point. This is shown for the case of PhCs formed using either expanded ($R_e > R_0$) or shrunken ($R_s < R_0$) unit cells in Fig. 1c-d. Using FDTD, we determine the bandwidth of the PhC bandgap for a perturbation of either $R_e/R_0 = 1.05$ or $R_s/R_0 = 0.94$ to be $\sim 20\text{THz}$ ($\sim 55\text{nm}$), centered at $\sim 330\text{THz}$ ($\sim 908\text{nm}$). For the simulations, we took $h=170\text{nm}$ and $s=140\text{nm}$. It is instructive to consider the nature of the bands in this case. For a shrunken (expanded) unit cell, the higher energy band has d -(p -) like character, and the lower energy band is p -(d -) like³. This difference in character has an important consequence when an interface is realised between the two unit cells (see Fig. 1e). The change in character of adjacent bands necessitates the formation of edge states, connecting bands of the same character across the interface. These can be clearly seen in the interface band structure shown in Fig. 1e. The edge states exist within the bandgap, and the interface therefore supports confined modes which form the basis of a topological photonic waveguide.

We harness the interface edge modes to create an optical ring resonator. A hexagonal array of expanded unit cells ($R_e/R_0 = 1.05$) is embedded within a host array of shrunken unit cells ($R_s/R_0 = 0.94$), as shown in Fig. 2a. (In the following, this corresponds to a perturbation of 5.5%.) Internally, each side of the resonator is 8 unit cells in length, such that the total path length of the interface is $\sim 21\mu\text{m}$. FDTD simulations of the resonator reveal a characteristic Fabry-Pérot spectral mode

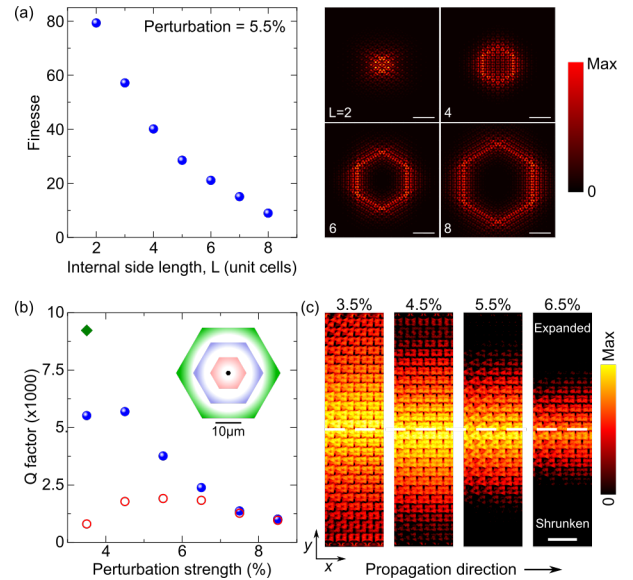


FIG. 3. (a) Simulated ring resonator finesse versus side length L (the number of internal unit cells at the interface) for a PhC perturbation of 5.5%. The corresponding electric field intensity profiles are shown to the right (linear scale). Scale bar $2\mu\text{m}$. (b) Simulated Q factor versus perturbation for a resonator with $L = 2$. The Q factor is independently evaluated for a host PhC with a side length of 16 unit cells (open red circles), 32 unit cells (filled blue circles) or 42 unit cells (filled green diamond). The inset shows the respective sizes of the resonator PhC (black hexagon) and the host PhC (larger hexagon, colour coded) in each case. (c) Simulated spatially-resolved electric field intensity for waveguides with perturbations of 3.5% to 6.5%, on a logarithmic intensity scale. The mode propagates in the x direction, as indicated. The unit cell is expanded (shrunken) above (below) the interface, which is highlighted by the dashed white line. Scale bar $1\mu\text{m}$.

structure (Fig. 2b), which lies within the topological bandgap (determined by monitoring the power radiated by a dipole source in an expanded-unit-cell PhC). Spatial intensity profiles of the modes as a function of wavelength are shown in Fig. 2c. Fabry-Pérot modes within the bandgap show strong confinement at the resonator interface, while non-guided bulk modes are evident outside of the bandgap.

Next, we investigate the theoretical dependence of the resonator finesse (quality factor (Q factor) multiplied by free spectral range, divided by mode frequency) on the device dimensions. Fig. 3a shows that for a resonator with an internal side length of $L = 8$ unit cells, embedded in a host PhC of shrunken unit cells with side length of $L = 16$ unit cells (as considered in Fig. 2, and later considered experimentally), the simulated finesse for the highest Q factor mode is ~ 10 (Q factor ~ 800). The finesse increases to ~ 80 (Q factor $\sim 1,900$) for a ring with an internal side length of 2 unit cells. Simulated mode profiles for resonators with $L = 2, 4, 6$ and 8 unit cells are also shown in Fig. 3a.

Now we fix the internal size of the ring at 2 unit cells,

and vary the perturbation (see Fig. 3b). When the size of the host PhC remains fixed at $L = 16$ unit cells, a peak in the Q factor is predicted for a perturbation of 5.5%. The peak arises due to competition between two effects. First, the propagation length of the waveguide mode decreases with increasing perturbation,⁴ explaining the reduction in Q factor for perturbations larger than 5.5%. Second, the spatial confinement of the modes reduces as the perturbation reduces. This means that for the smallest perturbations, the resonator mode begins to leak out of the host PhC into the surrounding membrane (as evident from the mode profiles shown in Fig. 3c). Therefore, the Q factor also reduces if the perturbation is very small. To demonstrate this more clearly, the simulations are repeated using a host PhC with a side length of $L = 32$ unit cells. The resonator Q factor is seen to increase most significantly for the smallest perturbations, implying reduced loss into the surrounding membrane. Computational restrictions prevent our use of FDTD to determine the ultimate Q factor for the resonator embedded in an infinite host PhC, but a lower limit of $\sim 9,200$ is obtained when the host PhC is increased in size to $L = 42$ unit cells, for a perturbation of 3.5%.

Experimentally, we fabricate topological ring resonators in a nominally 170nm-thick GaAs membrane, using standard electron beam lithography and dry etching techniques. A scanning electron microscope (SEM) image of a representative ring resonator is shown in Fig. 4a. The resonator has an internal side length of 8 unit cells, and is embedded in a host PhC with a side length restricted to 16 unit cells due to experimental limitations. Devices are fabricated with perturbation between 2.5% ($R_e/R_0 = 1.02$, $R_s/R_0 = 0.97$) and 5.5% ($R_e/R_0 = 1.05$, $R_s/R_0 = 0.94$).

To characterise the devices, the sample is mounted in an exchange gas cryostat, and the waveguide modes of the resonator are probed using micro-photoluminescence (μ -PL) spectroscopy. We use an excitation wavelength of 808nm, and focus the laser to a spot size of $\sim 2\mu\text{m}$. High power excitation is used to generate broadband emission from the QD ensemble. Mirrors in the collection path, with motorized adjusters, enable the collection of PL emission from a location either coincident with, or spatially distinct from, the excitation spot. We first position the excitation laser spot on one side of the ring (region ‘b’ in Fig. 4a), and detect light emitted from a location on the opposite side of the resonator (region ‘Col’ in Fig. 4a). This enables us to detect light coupled to the interface, whilst rejecting PL which is emitted into free space modes. The PL spectrum for a ring resonator with a unit cell perturbation of 5.5% is shown in Fig. 4b. Fabry-Pérot modes with a period of $\sim 7\text{nm}$ are observed, consistent with the round-trip path length of the resonator. The modes have Q factors in the range 200-500, possibly limited by dopant-related absorption in the GaAs membrane.

We next excite PL at several other positions on the resonator interface while collecting from the same loca-

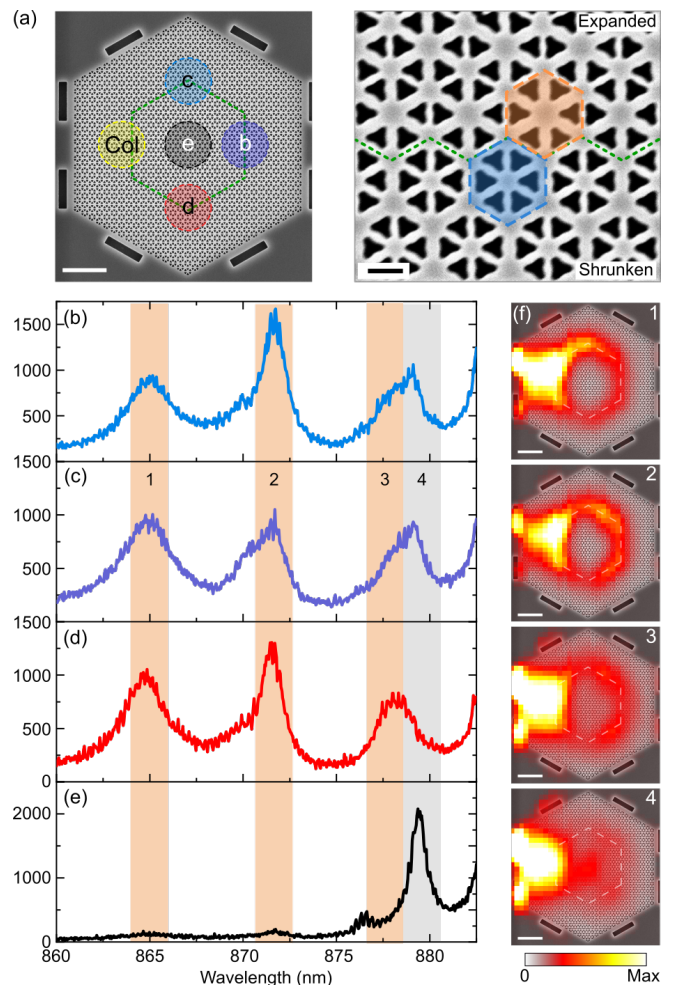


FIG. 4. (a) Scanning electron microscope (SEM) overview of the ring resonator (left, scale bar $2\mu\text{m}$) and close up of the waveguide interface (right, scale bar 200nm). (b-e) PL spectra for four different excitation locations on the device, as labelled in (a). In each case, the collection spot was fixed on the left hand side of the resonator (yellow circle labelled ‘Col’ in (a)). (f) Spatially-resolved, integrated PL intensity maps for four different bandwidths, as numbered and highlighted in (b-e). An SEM image of the device is positioned under each map, and the interface highlighted with a dashed white line. The zero of the linear colour scale is transparent. Scale bar $2\mu\text{m}$.

tion as previously, and observe that the mode structure remains unchanged (see Fig. 4c-d). However, when the excitation location is distinct from the interface (for instance, at the very centre of the resonator), the PL spectrum is quite different, and the modes observed previously at the interface are absent (Fig. 4e). This is strong evidence that the modes are confined to the interface. (A different peak is seen in Fig. 4e). We show below that this is distinct from the resonator modes.)

To visualise the modes more clearly, we raster scan the excitation laser across the device, simultaneously acquiring PL spectra from the same (fixed) collection spot used above. For each excitation position on the device,

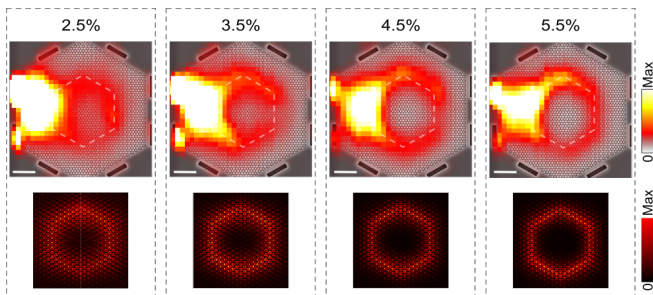


FIG. 5. Dependence of waveguide mode confinement on perturbation. Upper panels: Spatially-resolved, integrated PL intensity maps for different unit cell perturbations (as labelled). The integration is for a mode centered at ~ 865 nm in each case. An SEM image of the device is positioned under each map, and the interface highlighted with a dashed white line. The zero of the linear colour scale is transparent. Scale bar $2\mu\text{m}$. Lower panels: Simulated spatially-resolved electric field intensity (linear scale) of a representative ring resonator mode, for devices with the same perturbations as in experiment.

we sum the measured PL intensity over three different bandwidths corresponding to the different Fabry-Pérot modes seen in Fig. 4b-d. The resulting PL intensity maps are shown in Fig. 4f. Several features are apparent in the data. Most significantly, PL emission is observed from all positions along the resonator interface, with a clear node in the centre of the resonator, showing that light is guided along the interface. A secondary feature is the bright region on the left of each intensity map, an artifact of the measurement protocol which corresponds to the PL collection location. The PL maps also serve to highlight the location of trenches used to aid fabrication of the device (for instance, the two bright regions to the left of the collection location). These were used to accurately position the device schematic over each PL map. In Fig. 4f we also show an intensity map integrated over the single peak seen in the PL spectrum from the centre of the device. The map is quite different to those for the Fabry-Pérot modes seen at the interface, as this peak is not related to guided modes at the interface.

Finally, we investigate the effect of the unit cell perturbation on the spatial confinement of the resonator modes. Fig. 5a shows an integrated PL intensity map for each of four different ring resonators, with unit cell perturbation increasing from 2.5% to 5.5%. In each case, the intensity map corresponds to a single resonator mode, centered at ~ 865 nm. A clear trend is observed, with the mode confinement being strongest for the largest perturbation, and weakening with decreasing perturbation. For a perturbation of 5.5%, the mode decays over a distance of $2.7 \pm 0.1\mu\text{m}$, transverse to the propagation direction. This value increases to $4.1 \pm 0.2\mu\text{m}$ for a perturbation of only 2.5%. The change in confinement is consistent with FDTD simulations (see Fig. 3 and Fig. 5b), which show that, as the perturbation is decreased, the waveguide mode increasingly extends into the bulk PhC. From

the simulations, we estimate that the spatial extent of the mode normal to the propagation direction increases from ~ 820 nm for a perturbation of 5.5% to ~ 1640 nm for a perturbation of 2.5%. (The discrepancy between experiment and simulation is due to convolution of the experimental data with the laser spot size of $\sim 2\mu\text{m}$.) This suggests a robust method to tune the degree of evanescent coupling between the ring resonator and an adjoining bus waveguide, for instance in an add-drop filter. The perturbation is dependent on the location of the triangular apertures forming the PhC. This is simple to control lithographically, unlike the case of devices which rely on fine tuning of the resonator-waveguide spacing.

In conclusion, we have created a GaAs spin Hall topological photonic ring resonator, and used embedded InGaAs QDs to probe the mode structure of the device. Using spatially resolved PL measurements, we demonstrated that the modes were confined to the PhC interface. Furthermore, we showed that by controlling the perturbation of the PhC unit cell, the spatial confinement of the modes could be tuned. The resonator represents an important building block in the development of integrated photonic devices using embedded quantum emitters.

Data supporting this study are openly available from the University of Sheffield repository.²¹

This work was supported by EPSRC Grant No. EP/N031776/1.

- ¹C. P. Dietrich, A. Fiore, M. G. Thompson, M. Kamp, and S. Höfling, “GaAs integrated quantum photonics: Towards compact and multi-functional quantum photonic integrated circuits,” *Laser & Photonics Reviews* **10**, 870–894 (2016).
- ²M. C. Rechtsman, J. M. Zeuner, Y. Plotnik, Y. Lumer, D. Podolsky, F. Dreisow, S. Nolte, M. Segev, and A. Szameit, “Photonic Floquet topological insulators,” *Nature* **496**, 196–200 (2013), 1212.3146.
- ³S. Barik, H. Miyake, W. DeGottardi, E. Waks, and M. Hafezi, “Two-dimensionally confined topological edge states in photonic crystals,” *New Journal of Physics* **18**, 113013 (2016).
- ⁴S. Barik, A. Karasahin, C. Flower, T. Cai, H. Miyake, W. DeGottardi, M. Hafezi, and E. Waks, “A topological quantum optics interface,” *Science* **359**, 666–668 (2018).
- ⁵Y. Yang, H. Jiang, and Z. H. Hang, “Topological Valley Transport in Two-dimensional Honeycomb Photonic Crystals,” *Scientific Reports* **8**, 1588 (2018).
- ⁶Y. Yang and Z. H. Hang, “Topological whispering gallery modes in two-dimensional photonic crystal cavities,” *Optics Express*, Vol. 26, Issue 16, pp. 21235–21241 **26**, 21235–21241 (2018).
- ⁷L.-H. Wu and X. Hu, “Scheme for Achieving a Topological Photonic Crystal by Using Dielectric Material,” *Physical Review Letters* **114**, 223901 (2015).
- ⁸A. B. Khanikaev and G. Shvets, “Two-dimensional topological photonics,” *Nature Photonics* **11**, 763–773 (2017).
- ⁹R. E. Christiansen, F. Wang, O. Sigmund, and S. Stobbe, “Designing photonic topological insulators with quantum-spin-Hall edge states using topology optimization,” *Nanophotonics* **8**, 1363–1369 (2019).
- ¹⁰P. D. Anderson and G. Subramania, “Unidirectional edge states in topological honeycomb-lattice membrane photonic crystals,” *Optics Express* **25**, 23293 (2017).
- ¹¹L. Lu, J. D. Joannopoulos, and M. Soljačić, “Topological photonics,” *Nature Photonics* **8**, 821–829 (2014).
- ¹²T. Ozawa, H. M. Price, A. Amo, N. Goldman, M. Hafezi, L. Lu, M. C. Rechtsman, D. Schuster, J. Simon, O. Zilberberg,

- and I. Carusotto, “Topological photonics,” *Reviews of Modern Physics* **91**, 015006 (2019).
- ¹³X.-C. Sun and X. Hu, “Topological Ring-Cavity Laser Formed by Honeycomb Photonic Crystals,” (2019), arXiv:1906.02464.
- ¹⁴T. Yamaguchi, Y. Ota, R. Katsumi, K. Watanabe, S. Ishida, A. Osada, Y. Arakawa, and S. Iwamoto, “GaAs valley photonic crystal waveguide with light-emitting InAs quantum dots,” *Applied Physics Express* **12**, 062005 (2019).
- ¹⁵M. I. Shalaev, W. Walasik, A. Tsukernik, Y. Xu, and N. M. Litvinchits, “Robust topologically protected transport in photonic crystals at telecommunication wavelengths,” *Nature Nanotechnology* **14**, 31–34 (2019).
- ¹⁶X.-T. He, E.-T. Liang, J.-J. Yuan, H.-Y. Qiu, X.-D. Chen, F.-L. Zhao, and J.-W. Dong, “A silicon-on-insulator slab for topological valley transport,” *Nature Communications* **10**, 872 (2019).
- ¹⁷M. Hafezi, S. Mittal, J. Fan, A. Migdall, and J. M. Taylor, “Imaging topological edge states in silicon photonics,” *Nature Photonics* **7**, 1001 (2013).
- ¹⁸S. Barik, A. Karasahin, S. Mittal, E. Waks, and M. Hafezi, “Chiral quantum optics using a topological resonator,” (2019), arXiv:1906.11263.
- ¹⁹P. Lodahl, S. Mahmoodian, S. Stobbe, A. Rauschenbeutel, P. Schneeweiss, J. Volz, H. Pichler, and P. Zoller, “Chiral quantum optics,” *Nature* **541**, 473 (2017).
- ²⁰“Lumerical Inc.” <https://www.lumerical.com/products/>, accessed: 16-09-2019.
- ²¹<https://doi.org/10.15131/shef.data.9944957>.